Chinese Chemical Letters 33 (2022) 442–446

Contents lists available at ScienceDirect

Chinese Chemical Letters

journal homepage: www.elsevier.com/locate/cclet

Sunlight photocatalytic degradation of ofloxacin using UiO-66/wood composite photocatalysts

Linhong Shi[a], Xue Zou[a], Tengfei Wang[a], Dongmei Wang[a], Meikun Fan[a,b], Zhengjun Gong[a,b,*]

[a] Faculty of Geosciences and Environmental Engineering, Southwest Jiaotong University, Chengdu 611756, China
[b] State-province Joint Engineering Laboratory of Spatial Information Technology of High-Speed Rail Safety, Chengdu 611756, China

ARTICLE INFO

Article history:
Received 9 February 2021
Revised 1 May 2021
Accepted 16 June 2021
Available online 24 June 2021

Keywords:
Photocatalytic degradation
Metal-organic frameworks
Ofloxacin
Antibiotic
Water pollution

ABSTRACT

This study synthesized UiO-66 (Zr) *in situ* on wood *via* a one-step solvothermal method. UiO-66/wood was successfully prepared and its catalytic performance for the ofloxacin (OFX) photodegradation under simulate sunlight was also explored. UiO-66/wood exhibited a better catalytic performance, and its degradation rate constant was about 1.2 and 1.5 times than that of UiO-66 and wood, respectively. The effects of solution initial concentration, pH of the system and dosage of the photocatalyst were explored. Additionally, the active species trapping experiments and UV–vis diffused reflectance spectra measurements were conducted to investigated the photocatalytic mechanism of the UiO-66/wood composite, superoxide radical ($O_2^{\bullet-}$) and hydroxyl radical ($^{\bullet}OH$) were the main reactive species. In addition, the possible degradation pathways of OFX were analyzed by LC-MS. Meanwhile, the UiO-66/wood showed outstanding stability and reusability after 4 cycles experiments. The removal performance of UiO-66/wood towards real samples showed it has potential in actual application .

Antibiotics are generally used to treat animals and humans infections which are caused by anaerobic and protozoan bacteria [1]. The harm of antibiotics has attracted worldwide attention due to their durability, high toxicity and solubility in water, as well as complex molecular structures [2]. Antibiotics may lead to the emergence of a new antibiotic resistant bacteria which can eventually threaten human health [3]. Fluoroquinolones (FQs) mainly include ofloxacin, clinafloxacin, norfloxacin and ciprofloxacin, are widely diffused in environmental aqueous matrices. At present, various FQs have been detected at obvious concentrations in environmental media because of the low biodegradability and stable chemical structures [4].

Thus, versatile methods were extensively studied for the degradation FQs from water, such as biological treatments [3], adsorption [5], electrochemical treatment [6], photocatalysis (PC) [7], advanced oxidation processes (AOPs) [8]. Photocatalysis is an ideal method owing to the high efficiency, low energy consumption and environmentally friendly. The photocatalytic reaction conditions mainly include UV light irradiation, visible light irradiation, and simulated sunlight irradiation. Among them, thanks to the mild reaction conditions and low energy consumption, the photocatalytic reaction under simulative sunlight irradiation has great potential in practical applications. Over the years, several researches have shown the combination of adsorption and photocatalysis technology can enhance the degradation effect of pollutants [2,9,10].

Metal organic frameworks (MOFs) are a unique hybrid porous crystalline solid comprised of organic ligands and metal clusters (or metal cations). MOFs have high surface area, framework flexibility, structural diversity and tunable structures [11]. The outstanding characteristics make MOFs widely used in drug delivery [12], gas storage, sensing [13], storage/separation [14] and catalysis [10]. In recent years, MOFs based catalysts are applied to environmental pollutant degradation [15,16], hydrogen evolution [17], and carbon dioxide reduction [18]. Among various MOFs, UiO-66 series are of especially concern thanks to their excellent properties such as water stability. In 2019, UiO-66/wood membrane prepared by encapsulating UiO-66 in basswood showed high efficiency removal for organic pollutant in water [19]. ZnTCPc/UiO-66 (NH_2) was applied to methylene blue degradation under visible-light irradiation [20]. The photocatalysts synthesized through ZIF-8 modified tubular g-C_3N_4 were used for CO_2 reduction [18]. Co-doped UiO-66 nanoparticle showed excellent adsorptive ability and photocatalytic performance towards tetracycline under simulative sunlight [2].

* Corresponding author.
E-mail address: gzj@home.swjtu.edu.cn (Z. Gong).

https://doi.org/10.1016/j.cclet.2021.06.048
1001-8417/

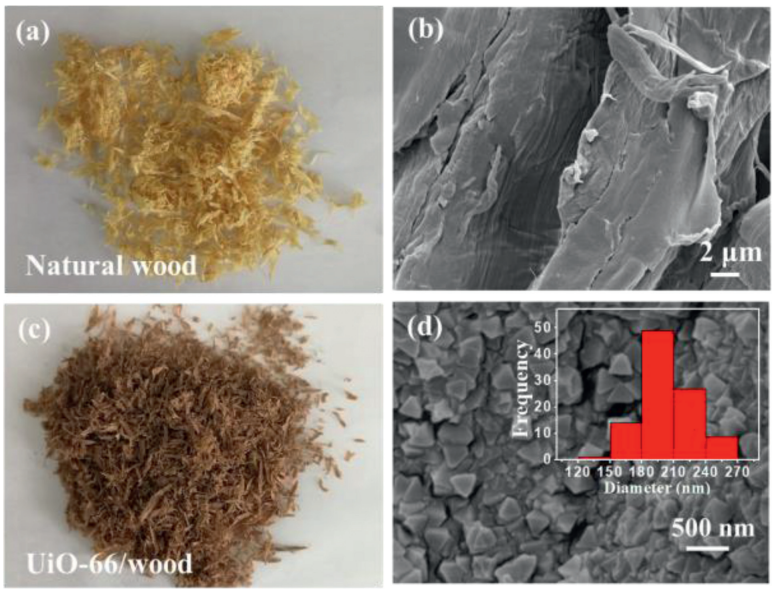

Fig. 1. (a) (c) Photos of the natural wood and UiO-66/wood. (b) Scanning electron microscope (SEM) image of the natural wood. (d) Magnified SEM image of the UiO-66 NPs in wood channels. Insert shows the size distribution of the UiO-66 NPs.

In the present paper, a novel photocatalyst UiO-66/wood was synthesized *via* a one-step solvothermal method, which was used as photocatalysts for ofloxacin (OFX) degradation under simulate sunlight irradiation. The open and aligned internal structure in wood, not only increasing the possibility of contact between photocatalyst and OFX, but also leading to the pre-concentration of OFX and is beneficial to the photocatalytic process. The influence of the reaction conditions including solution initial concentration, initial pH of the system and catalyst dosage were explored. The stability and reusability of UiO-66/wood are evaluated. Moreover, the possible mechanism and degradation pathways for OFX photodegradation were also studied.

The details of experimental section are deposited in Section S1 (Supporting information). Fig. 1b and Fig. S1 (Supporting information) show there are a large number of slender and irregular microchannels in natural wood. The photo images of the natural wood (light yellow) and UiO-66/wood (dark brown), respectively (Figs. 1a and c). Fig. S2 (Supporting information) shows the UiO-66 nanoparticles (UiO-66 NPs) are uniformly distributed on the multiple wood channels. It can be known that the shape of the UiO-66 NPs is cuboid and the size of the UiO-66 NPs is about 204 ± 25 nm (Fig. 1d). The energy dispersive X-ray spectrometer (EDX) spectra shows there are three elements of Zr, C and O in UiO-66 wood (Fig. S3 in Supporting information).

X-ray diffraction patterns (XRD) spectra can analyze the composition and crystallinity of the prepared samples. The XRD spectra of natural wood, UiO-66, and UiO-66/wood are shown in Fig. S4 (Supporting information). Comparing with previous studies, the characteristic peaks of UiO-66 are in good agreement [21,22], indicating that UiO-66 was successfully prepared. Because the low crystallinity of natural wood, and the UiO-66 NPs are uniformly distributed on the wood channels, the crystallinity of the UiO-66/wood is poor. The result demonstrates the XRD pattern of the UiO-66/wood is match well with UiO-66 and wood, and mainly consistent with the wood.

The Raman spectra of the UiO-66 is shown in Fig. S5 (Supporting information). In the 600–1700 cm^{-1} range, there are many peaks ascribed to BDC organic linkers [20]. The vibrations at 600–900 cm^{-1} are attributed to out-of-plane bending of C–H bonds. The bands at 1140 cm^{-1} and 1400–1620 cm^{-1} are assigned to in-plane bending of C–H bonds and stretching of C–C bonds, respectively [23]. From the Fourier transform infrared spectroscopy (FT-IR) spectra shown in Fig. S6 (Supporting information), the small band at 1660 cm^{-1} can be assigned to the asymmetric expansion of C=O bonds due to the residual dimethyl formamide (DMF) [23]. The bands at 1401 cm^{-1} and 1590 cm^{-1} belong to the symmetric and asymmetric stretch vibrations of OCO in H_2BDC, respectively [24]. The band at 1510 cm^{-1} represents the C = C vibration in the benzene ring [25]. At lower frequencies, the band around 748 cm^{-1} is mixed with the vibration of C–H vibration and stretch of C=C stretch in H_2BDC [24]. The band at 550 cm^{-1} is attributed to the asymmetric stretch of Zr-(OC) [25,26]. There is a representative absorption band around 484 cm^{-1}, which is owing to the NH_2-BDC [27]. Therefore, the synthesis of the UiO-66/wood is proved by the results of XRD, EDX and FT-IR.

The surface morphology and pore volume of UiO-66/wood and UiO-66 are observed by nitrogen physisorption method. The physicochemical parameters of the photocatalysts are shown in Fig. S7 and Table S1 (Supporting information). It is found that all the UiO-66 and UiO-66/wood display a type I isotherm, indicating their microporous characteristics. From Table S1, the porosity of the UiO-66/wood is obviously less than that of UiO-66, which could be ascribed to the partial coverage of UiO-66 by wood.

In order to study the separation and recombination of electron hole pairs in photocatalysts, the photoluminescence (PL) spectra of three catalysts are measured in Fig. S8 (Supporting information). Generally speaking, the combination of photo-generated electron hole pairs releases energy to form PL emission, thus reducing photocatalytic performance [28]. Comparing with UiO-66, the PL intensity of UiO-66/wood is lower, which means the existence of wood can reduce the recombination rate of photogenerated electron hole pairs and improve the properties of the photocatalyst.

Fig. 2a depicts the performance of UiO-66, wood and UiO-66/wood for the OFX photocatalytic degradation under simulated sunlight. Before simulated sunlight irradiation, the system was stirred slowly in the dark for 90 min to reach the adsorption-desorption equilibrium (Fig. S9 in Supporting information). As shown in Fig. 2a, without a photocatalyst, OFX self has a weak degradation effect under sunlight. Comparing with other catalysts, UiO-66/wood shows the best photodegradation properties on OFX. The OFX photodegradation confirms to the pseudo-first-order model, so the reaction rate constants (k) value is calculated

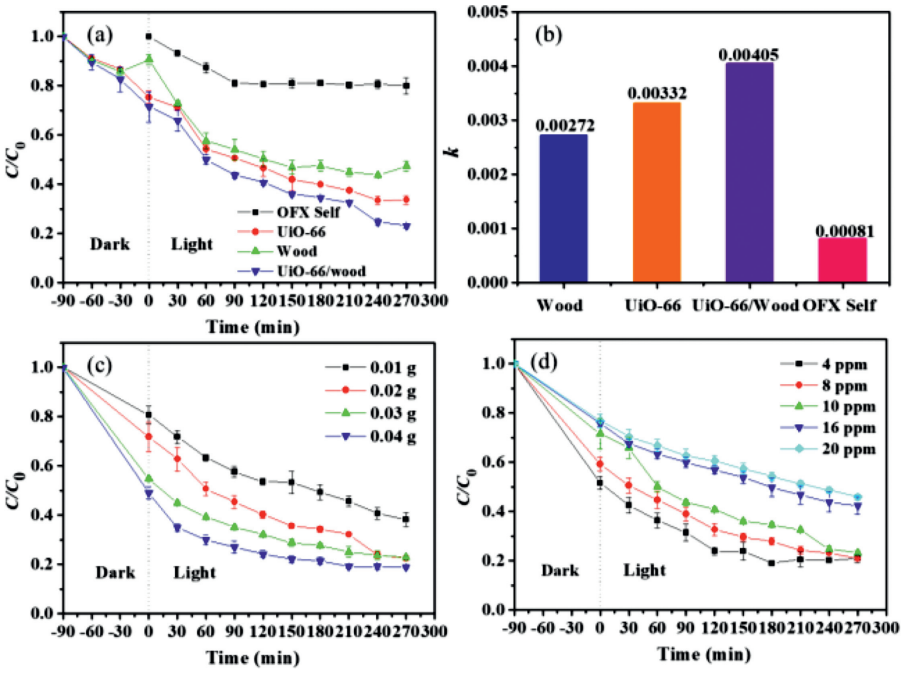

Fig. 2. Comparison of catalytic curves (a) and (b) k value of different photocatalysts for OFX degradation. Reaction conditions: OFX (10 mg/L, 35 mL); catalyst dosage (0.02 g); initial pH = 6. Influences of reaction conditions on the experiment: (c) amount of catalyst (d) initial concentration.

based on the *pseudo*-first-order kinetic equation: $\ln(C_0/C) = kt + A$ (Fig. 2b). According to the k value, the photocatalytic properties of each catalyst follow the order UiO-66/wood (40.5×10^{-4} min^{-1}) > UiO-66 (33.2×10^{-4} min^{-1}) > wood (27.2×10^{-4} min^{-1}) > OFX self (8.10×10^{-4} min^{-1}).

The influence of catalyst dosage is shown in Fig. 2c. As the catalyst dosage increasing, the total surface area and active sites of the photocatalysts also increased. The photocatalysts can capture further photogenerated electrons to generated more active radicals. Nevertheless, when the catalyst dosage increasing from 0.02 g to 0.04 g, this phenomenon was only noted before the reaction time was 240 min. The dosage effect would be ignored while the reaction time changing to 270 min. This phenomenon would be possibly explained as sunlight penetration decrease caused by lots of photocatalysts dispersed in solution.

The solution initial concentration is a crucial parameter. As showed in Fig. 2d, the OFX concentration had impact on the degradation process, where 80.96%, 78.8%, 76.87%, 57.58%, and 54.8% of OFX were removed at OFX concentration of 4, 8, 10, 16 and 20 ppm, respectively. As the OFX level in the aqueous phase increases, the concentrations will become surplus. In this case, some of the OFX can only interact with insufficient active sites on the catalyst surface, which will reduce the efficiency of OFX degradation at higher initial concentrations.

The effect of initial solution pH on OFX photodegradation was estimated in the range of pH 2.0–10.0 (Fig. S10 Supporting information). In addition to the generation of radicals during the photocatalytic process, there is also electrostatic interaction between the photocatalyst and the reaction substrate. Therefore, it is hard to analyze how the pH affects the reaction process [29]. While the pH increasing from 2 to 8, the degradation rate of OFX gradually increasing. The degradation rate does not increase significantly from pH 8–10, which might because the decreased solubility of OFX in this pH range. Meanwhile, the UiO-66 tends to dissolve at pH higher than 9, which further leading to the phenomenon.

The reusability and stability of photocatalysts are among the key factors for long time applications. As shown in Fig. S11 (Supporting information), the photocatalytic performance of UiO-66/wood does not obviously decrease after four recycles. Moreover, the XRD patterns of UiO-66/wood of fresh and after repeat 4 times further indicating UiO-66/wood has nice stability during OFX degradation process (Fig. S12 Supporting information).

Table S2 (Supporting information) shows a short overview of OFX degradation and our work. Compared with other processes, the UiO-66/wood used in this study is synthesized *via* a simple one-step hydrothermal method, which is easy to separate and recycle. In addition, the degradation of OFX is under sunlight irradiation, which is conducive to practical applications. Moreover, the UiO-66/wood showed excellent stability and reusability in circulation experiments. Therefore, it shows great potential in actual wastewater treatment.

The reactive species trapping experiments were carried out to investigate the photocatalytic mechanism of the UiO-66/wood composite. Three different scavengers, sodium oxalate, *p*-benzoquinone (BQ) and methanol, were employed as scavengers for H^+, $O_2^{\bullet-}$ and $^{\bullet}OH$, respectively [20,30]. As show in Figs. S13a and b (Supporting information), the photocatalytic activity of UiO-66/wood was promoted in the presence of sodium oxalate. This phenomenon may be due to the presence of sodium oxalate, the H^+ radical scavenger was captured, thereby generating more electrons. Molecule oxygen adsorbed on UiO-66 can be restored to $O_2^{\bullet-}$, and then promote the photocatalytic process. Nevertheless, the photodegradation efficiency significantly decrease after adding methanol and BQ, the degradation rate was only 17.8% in the presence of methanol. These phenomena indicate the roles of $O_2^{\bullet-}$ and $^{\bullet}OH$ as the key reactive species in OFX photodegradation.

The optical characteristics of synthesized samples were recorded by the UV–vis DRS. It can be seen from Fig. S13c (Supporting information), the absorption edge at 310 nm of UiO-66 spectrum can be attributed to π-π^* electronic transitions of the aromatic ring [20]. The UiO-66 has not significant absorption in the range of 350–800 nm, suggesting it cannot utilize photo-energy in the visible light region. In contrast, natural wood and the UiO-66/wood have a response to visible light.

The E_g of the UiO-66/wood and UiO-66 were 3.67 and 3.89 eV, respectively (Fig. S13d in Supporting information). According to the

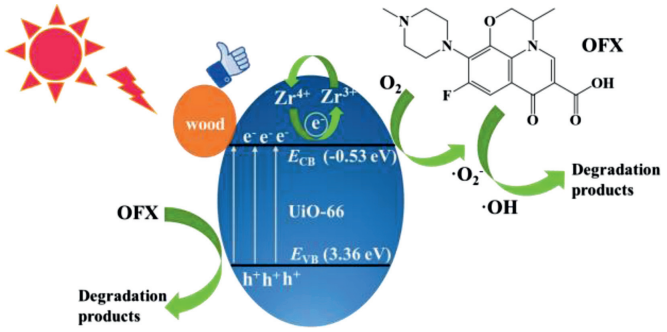

Fig. 3. A schematic illustration of photocatalytic degradation of OFX over UiO-66/wood under sunlight irradiation.

previous report, the flat band position of UiO-66 is −0.33 eV *vs.* NHE [21]. The flat band potential of n-type semiconductor is 0.2 V lower than the E_{CB} [31]. Therefore, the E_{CB} of UiO-66 is −0.53 eV *vs.* NHE, the valence band position (E_{VB}) of UiO-66 is 3.36 eV *vs.* NHE. On the basis of those results and analysis, the possible photocatalytic mechanism is proposed and illustrated in Fig. 3. The porous structure of UiO-66/wood allows OFX molecules to be adsorbed on the surface and promotes the photocatalytic process. The photo-induced electron derived from the organic ligands transfer to the Zr-O oxo-cluster of the UiO-66 then form Zr^{3+}under simulative sunlight [21]. Molecule oxygen adsorbed on UiO-66, the as-formed Zr^{3+} could react with O_2 to form $O_2^{\bullet-}$, while Zr^{3+} is oxidized to Zr $^{4+}$ [21,32,33]. The electrons transportation *via* the presence of Zr^{3+}-Zr^{4+} intervalence electron transfer had been demonstrated by previous studies [34]. Meanwhile, H_2O molecule adsorbed on UiO-66 are oxidized to $^{\bullet}OH$ by the photo-generated holes. Finally, the $O_2^{\bullet-}$ and $^{\bullet}OH$ degrade OFX molecules. The existence of wood can accelerate the rate of photogenerated electron capture, thereby inhibiting the combination of photogenerated electron-hole pairs, which improving photocatalytic performance.

The LC-MS was used to monitor the OFX photodegradation intermediates and explored the probable degradation pathway (Fig. S14 in Supporting information). Table S3 (Supporting information) shows the possible transformation products. Based on Table S3, there are two probable pathways (Fig. 4). Pathway I was the demethylation reaction, which was extensively reported for photolysis of FQs [35]. Under sunlight irradiation, the OFX was attacked by $^{\bullet}OH$, which releasing the $-CH_3$ and forming **P1**. Subsequently, **P1** was successively attacked by $^{\bullet}OH$ and underwent dehydrogenation to produce **P2**. Then **P3** can be generated through defluorination of the **P2** [36]. In pathway II, $^{\bullet}OH$ attacked on OFX, the product **P** was formed by effectively releasing the *N*-methylpiperazine [30]. Although the product was not monitored in this research, its existence cannot be ruled out. As shown, the product **P** loss a carbonyl moiety, CO_2 and 2 hydrogens, causing a double bond to form in the methyl group, which formed the **P4** [36]. The **P3** and **P4** can be further oxidized and formed **P5**. Ultimately, the above products (**P1**, **P2**, **P3**, **P4** and **P5**) will be transformed into H_2O and CO_2.

Escherichia coli were sensitive to fluoroquinolone antibiotics, which could be used to the toxicity evaluation of intermediate products generated during the process of OFX photodegradation [32,37]. In Fig. S15 (Supporting information), the inhibition zone diameters of initial OFX solution were 23 mm (the average value of four inhibition zones), which showed the obvious antibacterial effect of OFX. After the photodegradation for 240 min on UiO-66/wood, the inhibition zone diameters were 9 mm (the average value of four inhibition zones). The reduced inhibition zone area indicated that the toxicity of degradation products was lower than initial contaminants in this study.

The application of UiO-66/wood in the treatment of actual samples was investigated in Fig. S16 (Supporting information). After dark adsorption and simulated sunlight irradiation, the degradation rate of ofloxacin (prepared by ofloxacin tablets) in different actual samples were 60.9%, 46.2% and 38.6%, respectively. But the removal rate of ofloxacin (prepared by levofloxacin hydrochloride capsules) in different actual samples were 54.8%, 47.0% and 36.0%, respectively. This may be because the purity of ofloxacin in levofloxacin hydrochloride capsules is low, which affects the degradation effect. In general, the UiO-66/wood photocatalytic showed a good photocatalytic efficiency of OFX in real samples, which was potential in wastewater treatment.

In summary, a novel photocatalyst UiO-66/wood was synthesized *via* a one-step solvothermal method and used for OFX degradation under sunlight irradiation. According to the analysis of characterization results, the presence of wood can hinder the combination of photogenerated electron-hole pairs, thus improving the photocatalytic performance of UiO-66/wood. Meanwhile, the UiO-66/wood exhibited outstanding stability and reusability. The reactive species trapping experiments implied $O_2^{\bullet-}$ and $^{\bullet}OH$ could be the main active contributors. In addition, two probable degradation pathways of OFX were proposed, OFX will finally transformed into H_2O and CO_2. Moreover, the removal performance of UiO-66/wood towards real samples showed that it has potential in actual application.

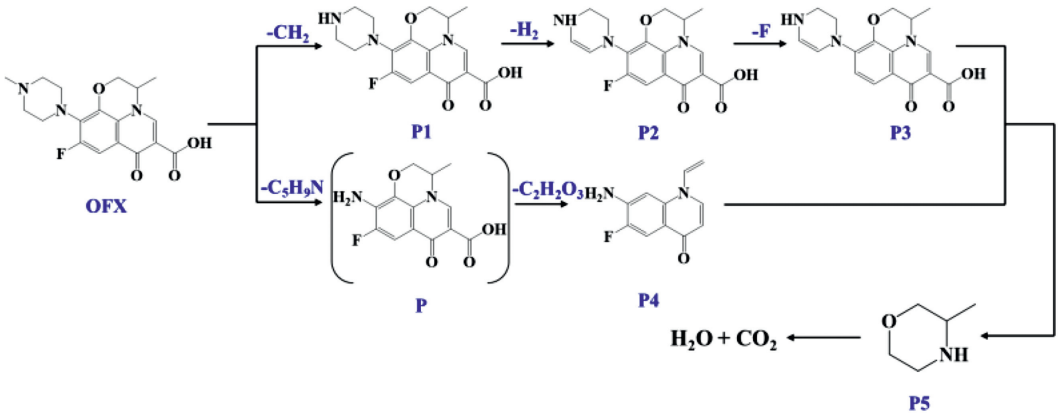

Fig. 4. The proposed transformation pathways of OFX degradation.

Declaration of competing interest

The authors declare that they have no known competing financial interests or personal relationships that could have appeared to influence the work reported in this paper .

Acknowledgments

The research was supported by the National Natural Science Foundation of China (Nos. 21777131 and 21677117), Science and Technology Department Foundation of Sichuan Province (Nos. 2018GZ0400 and 2018SZDZX0026), the Fundamental Research Funds for the Central Universities (No. A0920502052001–6). Sincerely thanks Analytical and Testing Center of Southwest Jiaotong University for the experimental conditions .

Supplementary materials

Supplementary material associated with this article can be found, in the online version, at doi:10.1016/j.cclet.2021.06.048.

References

[1] P.W. Seo, N.A. Khan, S.H. Jhung, Chem. Eng. J. 315 (2017) 92–100.
[2] J. Cao, Z.H. Yang, W..P. Xiong, et al., Chem. Eng. J. 353 (2018) 126–137.
[3] M. Sturini, A. Speltini, F. Maraschi, et al., Water Res. 46 (2012) 5575–5582.
[4] L. Ge, G. Na, S. Zhang, et al., Sci. Total Environ. 527-528 (2015) 12–17.
[5] F. Yu, Y. Li, S. Han, J. Ma, Chemosphere 153 (2016) 365–385.
[6] N. Barhoumi, L. Labiadh, M.A. Oturan, et al., Chemosphere 141 (2015) 250–257.
[7] M. Sturini, F. Maraschi, A. Cantalupi, et al., Materials (Basel) 13 (2020) 537–549.
[8] M.N. Corella-Ochoa, J.B. Tapia, H.N. Rubin, et al., J. Am. Chem. Soc. 141 (2019) 14306–14316.
[9] P. Chen, X. Liu, R. Jin, W. Nie, Y. Zhou, Carbohydr. Polym. 167 (2017) 36–43.
[10] Y. Zhang, J.B. Zhou, W.Q. Cai, J. Zhou, Z. Li, Appl. Surf. Sci. 430 (2018) 549–560.
[11] H.C. Zhou, J.R. Long, O.M. Yaghi, Chem. Rev. 112 (2012) 673–674.
[12] J.Q. Sha, X.H. Zhong, L.H. Wu, G.D. Liu, N. Sheng, RSC Adv. 6 (2016) 82977–82983.
[13] X.L. Hu, C. Qin, X.L. Wang, K.Z. Shao, Z.M. Su, Chem. Commun. 51 (2015) 17521–17524.
[14] J.R. Li, J. Sculley, H.C. Zhou, Chem. Rev. 112 (2012) 869–932.
[15] H. Wang, X.Z. Yuan, Y. Wu, et al., J. Hazard. Mater. 286 (2015) 187–194.
[16] Y. Zhang, J. Zhou, Q. Feng, X. Chen, Z. Hu, Chemosphere 212 (2018) 523–532.
[17] R. Wang, L.N. Gu, J.J. Zhou, et al., Adv. Mater. Interfaces 2 (2015) 37–41.
[18] S.W. Liu, F. Chen, S.T. Li, X.X. Peng, Y. Xiong, Appl. Catal. B 211 (2017) 1–10.
[19] R. Guo, X. Cai, H. Liu, et al., Environ. Sci. Technol. 53 (2019) 2705–2712.
[20] Q. Liang, M. Zhang, Z.H. Zhang, et al., J. Alloys Compd. 690 (2017) 123–130.
[21] X.D. Zhang, Y. Yang, W.Y. Huang, et al., Mater. Res. Bull. 99 (2018) 349–358.
[22] Z. Sha, H.S.O. Chan, J.S. Wu, J. Hazard. Mater. 299 (2015) 132–140.
[23] M. Kandiah, M.H. Nilsen, S. Usseglio, et al., Chem. Mater. 22 (2010) 6632–6640.
[24] Y.T. Han, M. Liu, K.Y. Li, et al., Inorg. Chem. Front. 4 (2017) 1870–1880.
[25] L. Valenzano, B. Civalleri, S. Chavan, et al., Chem. Mater. 23 (2011) 1700–1718.
[26] S. Chavan, J.G. Vitillo, D. Gianolio, et al., Phys. Chem. Chem. Phys. 14 (2012) 1614–1626.
[27] K. Vellingiri, P. Kumar, A. Deep, K.H. Kim, Chem. Eng. J. 307 (2017) 1116–1126.
[28] Q. Liang, J. Jin, M. Zhang, et al., Appl. Catal. B: Environ. 218 (2017) 545–554.
[29] P.Y. Motlagh, A. Khataee, T.S. Rad, A. Hassani, S.W. Joo, J. Taiwan Inst. Chem. Eng. 101 (2019) 186–203.
[30] P. Chen, L. Blaney, G. Cagnetta, et al., Environ. Sci. Technol. 53 (2019) 1564–1575.
[31] Y.P. Yuan, L.S. Yin, S.W. Cao, et al., Appl. Catal. B: Environ. 168-169 (2015) 572–576.
[32] G. Zhang, G. Kim, W. Choi, Energy Environ. Sci. 7 (2014) 954–966.
[33] H. Wang, X.Z. Yuan, Y. Wu, et al., Appl. Catal. B: Environ. 186 (2016) 19–29.
[34] X.Q. Xu, R.X. Liu, Y.H. Cui, et al., Appl. Catal. B: Environ. 210 (2017) 484–494.
[35] S. Kusari, D. Prabhakaran, M. Lamshoft, M. Spiteller, Environ. Pollut. 157 (2009) 2722–2730.
[36] E. Hapeshi, I. Fotiou, D. Fatta-Kassinos, Chem. Eng. J. 224 (2013) 96–105.
[37] R.K. Singh, L. Philip, S. Ramanujam, Water Res. 121 (2017) 20–36.